Check for updates

How to cite: *Angew. Chem. Int. Ed.* **2025**, *64*, e202519704
doi.org/10.1002/anie.202519704

Supercapacitors **Very Important Paper**

Pre-Polymerization and Pre-Etching Dominated by Carbon Dots to Fabricate the Sub-Nanometer Microporous Carbon for Supercapacitors

Xi-Rong Zhang, Bao-Juan Wang, Hao-Wen Sun, Yong-Gang Wang, and Huan-Ming Xiong**

Abstract: The self-templating method is a facile and low-cost strategy to synthesize porous carbon materials, but the obtained products usually have low yields, limited specific surface areas (SSAs), and broad pore size distributions. It is a great challenge for the self-templating method to prepare the sub-nanometer (0.5–1.0 nm) microporous carbon that is preferred for high-performance supercapacitors. In this study, carbon dots (CDs) are employed as the sole precursor to prepare porous carbon without using any activating agents. The obtained carbon materials have large SSA (2733.6 m^2 g^{-1}), high micropore area ratio (92.5%), high packing density (0.82 g cm^{-3}), high yield (12%), and concentrated sub-nanometer pore structure. The formation mechanism of such porous carbon and the unique functions of CDs as self-templates are interpreted by various characterizations. When used as electrodes for supercapacitors, this carbon material exhibits specific capacitance up to 639 F g^{-1} and is compatible with electrolytes of wide pH values and enlarged voltage windows (1.3–1.7 V). The symmetric devices assembled by such material exhibit low self-discharge behaviors, excellent energy densities (15.9–44.1 Wh kg^{-1}), and good cycling performance even under the commercial-level mass loading (10 mg cm^{-2}) on electrodes.

Introduction

Porous carbon materials, due to their large specific surface area (SSA), tunable pore structures, excellent stability, and rich surface chemistry,[1–3] have received wide research in catalyst supports, fluid adsorption and separation, energy storage devices, etc. Among the commercial energy storage devices, supercapacitors possess high power density, excellent rate performance, and ultra-long cycle life.[4–7] Most supercapacitors employ the porous carbon as electrodes,[8–10] and thus, the pore size distribution and porosity of the porous carbon are crucial for enhancing its performance in practical applications.[11,12] The optimal microporous carbon should have high density (>0.7 g cm^{-3}) and large specific surface area (SSA > 2000 m^2 g^{-1}), along with moderate nitrogen/oxygen functional groups for improving both hydrophilicity and pseudocapacitance. Particularly, the sub-nanometer (0.5–1.0 nm) pores are mostly effective for the ion desolvation and adsorption, facilitating the high volumetric energy density storage in supercapacitors.[13–15]

The traditional strategies for synthesizing porous carbon can be classified into the activation routes and the template methods, which are insufficient to produce the sub-nanometer microporous carbon materials on a large scale.[16] The activation routes require some highly corrosive chemical reagents (e.g., $ZnCl_2$, KOH) or high-temperature steams (e.g., CO_2, O_2, or H_2O) for etching carbon to produce micropores.[17–23] These corrosive reagents often damage the reaction apparatus, leading to high cost and low yield, while the steam etching process is time-consuming, resulting in carbon materials with low SSA and random pore size distributions.[24–26] The template methods employing soft or hard templates to synthesize carbon materials usually produce macroporous or mesoporous structures, leading to low volumetric capacitance of supercapacitors.[27,28] In addition, the process of synthesizing and removing templates is the most complex and time-consuming, which significantly increases the production cost and may require highly hazardous reagents like HF.[29,30] In contrast, the self-templating methods are more efficient and greener for producing microporous carbon. By directly calcining some precursors, such as biomass and metal-organic salts, microporous carbon can be synthesized facilely with few corrosive agents, without complex/expensive templates and highly toxic reagents.[31–35] However, biomass typically results in disordered pore structures. While selecting appropriate precursors can help mitigate this issue, the pore distributions of the resulting products remain limited by the raw materials, making the precise design difficult.[36,37] The product yield of metal organic salts (K^+, Na^+) is generally low (<4%), and the biomass-derived carbon materials always exhibit a limited SSA (<2000 m^2 g^{-1}) after direct calcination. Although recent studies suggest that the use of highly reactive alkali metals (Cs^+) can improve the results, it also introduces significant safety concerns.[9,24,38,39] Therefore, it is still a challenge to find suitable self-templating precursors for preparing microporous

[*] Dr. X.-R. Zhang, B.-J. Wang, H.-W. Sun, Prof. Y.-G. Wang, Prof. H.-M. Xiong
Department of Chemistry, Shanghai Key Laboratory of Electrochemical and Thermochemical Conversion for Resources Recycling, Fudan University, Shanghai 200438, P.R. China
E-mail: ygwang@fudan.edu.cn
hmxiong@fudan.edu.cn

Additional supporting information can be found online in the Supporting Information section

© 2025 Wiley-VCH GmbH

carbon with high packing density (>0.7 g cm^{-3}), large SSA (>2000 m^2 g^{-1}), high yield (>10%), high micropore area ratio (>90%), and especially rich sub-nanometer pores.

Carbon dots (CDs), including carbonized polymer dots (CPDs), are a type of organic–inorganic hybrid nanomaterial with complex structures intermediate between inorganic nanocrystals (hard templates) and organic polymers (soft templates).[40–42] Based on this unique merit of CDs, we used them as pore-makers to produce sub-nanometer porous carbon successfully. In the previous report,[43] CDs were employed as additives to crosslink polymers rather than primary materials, because the fluffy CDs powder decomposed and vaporized rapidly during calcination, resulting in a low yield of carbon less than 1%. Since the numbers of sub-nanometer pores were limited in the final products, the as-prepared sample had an SSA of 1020 m^2 g^{-1} and a specific capacity of 516 F g^{-1}. When the corrosive agent $ZnCl_2$ was used to improve SSA at 800 °C, the yield of the obtained porous carbon was very low. In addition, the as-prepared carbon electrodes performed poorly in the neutral electrolytes due to their inappropriate surface groups, limiting their practical applications.

In the present work, we developed a CDs-dominated pre-polymerization and pre-etching route to overcome the above problems, in which the well-designed CDs were used as the sole precursors to prepare porous carbon, and any corrosive activation at high temperature was never needed. In the pre-polymerization, the CDs crosslinked with each other to form a highly dense hydrogel, which ensured less weight loss during the subsequent calcination. During the pre-etching process, a diluted solution of alkaline was applied to break amide bonds in CDs, extract small fragments, and generate numerous micropores in the hydrogel. After calcination without any corrosive agents, the as-prepared samples have high micropore area ratios (92.5%–98.3%), tunable SSA (1000–3000 m^2 g^{-1}), high yields (10%–14%), high packing density (up to 0.82 g cm^{-3}), and abundant sub-nanometer pores. When the optimal samples are assembled into supercapacitors, their specific capacities reach 639 F g^{-1}, and the symmetric devices exhibit a wide pH applicability range and large voltage windows (1.3–1.7 V). Even at the high mass loadings (10 mg cm^{-2}) on the electrodes, the supercapacitors exhibit high energy density, low self-discharge, excellent rate performance, and strong cycling stability. Our present results expanded the knowledge of CDs in porous carbon synthesis by establishing CDs as the main role in the self-template methods.[44,45]

Results and Discussion

Experimentally, citric acid (CA) and polyethyleneimine (PEI) were used to synthesize CDs hydrothermally, which formed hydrogels in the subsequent pre-polymerization (Scheme 1). Energy dispersive spectroscopy (EDS) confirmed the uniform distribution of carbon (C), nitrogen (N), and oxygen (O) elements within the hydrogel (Figure S1). Afterwards, the above carbon dot hydrogels (CDHs) were pre-etched in a 2 M KOH aqueous solution at 90 °C and then washed with deionized water thoroughly and labeled as CDH-e. X-ray photoelectron spectra (XPS) of CDs, CDH, and CDH-e were measured to study their compositions. In Table S1, the potassium (K) content was detected to be only 0.1% in CDH-e, indicating the efficient removal of KOH by the washing process. Ultimately, the CDH-e was calcined without any activating agents at an appropriate temperature. For example, after calcination of the CDH at 800 °C, the obtained porous carbon was designated as CCDH-800.

The Transmission Electron Microscopy (TEM) images reveal the precursor CDs are monodispersed with an average size of about 5 nm (Figure S2), while their high-resolution TEM (HRTEM) images (Figure 1a) display a distinctive fringe distance of 0.21 nm, corresponding to the (100) plane of graphite.[46] The broad diffraction peak observed in the X-ray diffraction (XRD) patterns (Figure 1b) indicates the nanoscale size and low crystallinity of CDs.[47] Fourier transform infrared spectroscopy (FTIR, Figure 1c) reveals vibration bands at 3442, 1711, 1650, 1386, and 1189 cm^{-1}, corresponding to O─H/N─H, C═O, C═N, C─N, and C─O groups, respectively. The full XPS in Figure S3a reveals three main peaks: C 1s (286 eV), N 1s (400 eV), and O 1s (532 eV), with atomic proportions of 69.3%, 12.3%, and 18.5%, respectively. In the high-resolution spectrum (Figure S3b), the C 1s peak can be deconvoluted into four components corresponding to sp^2 carbon (C─C/C═C, 284.4 eV), sp^3 carbon (C─O/C─N, 285.3 eV), carbonyl carbon (C═O, 286.2 eV), and carboxyl carbon (COOH, 287.9 eV), respectively. The N 1s peak can be resolved into three distinct peaks (Figure S3c) at 398.7, 400.1, and 401.5 eV, representing the pyridinic N, the pyrrolic N, and the graphitic N, respectively.[48] The O 1s peak contains two components of C═O and C─O at 531.0 and 532.1 eV, respectively (Figure S3d). The above results confirm that CDs possess π-conjugated carbon cores and various surface groups, such as amine and carboxyl functional groups, which are the basis of the pre-polymerization and the pre-etching processes.

To clarify the mechanism of the pre-etching process, the fluorescence spectra (Figure S4) of CDs, the scanning electron microscopy images (SEM; Figure 1d,f), and TEM images (Figure S5) of CDH and CDH-e were examined and compared, respectively. The fluorescence of CDs was nearly eliminated after KOH etching, indicating the structure of CDs was significantly damaged. In addition, the initially smooth surface of the CDH hydrogel disappeared, and instead, a large number of wrinkles and pores on the CDH-e surface emerged, which is the most intuitive manifestation of the etching step. The pore size distribution curve calculated by the density functional theory (DFT) (Figure 1e) indicates that before etching the hydrogel has almost no pores, while after etching the hydrogel possesses lots of pores, primarily less than 20 nm, and the SSA is increased by over ten times, from 0.88 to 9.47 m^2 g^{-1} after the pre-etching process. After etching, the nitrogen adsorption–desorption isotherms (Figure S6) shifted from Type VI to Type I, indicating a transition from the adsorption on a non-porous solid surface to the microporous adsorption. To further investigate the etching impact on the calcination process, thermogravimetric analyses (TGA) were conducted on CDs, CDH, and CDH-e, respectively. The TG curves (Figure 1g) reveal that before 150 °C, the weight loss

© 2025 Wiley-VCH GmbH

15213773, 2025, 50, Downloaded from https://onlinelibrary.wiley.com/doi/10.1002/anie.202519704 by Huan-Ming Xiong - Fudan University , Wiley Online Library on [12/12/2025]. See the Terms and Conditions (https://onlinelibrary.wiley.com/terms-and-conditions) on Wiley Online Library for rules of use; OA articles are governed by the applicable Creative Commons License

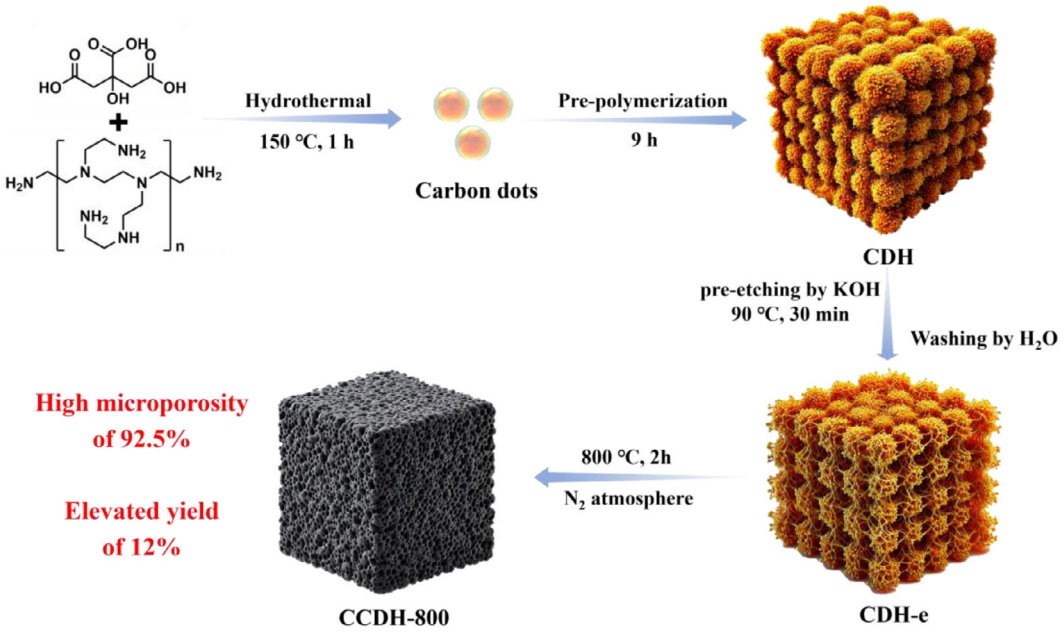

Scheme 1. Schematic diagram of the synthetic procedure for CCDH-800.

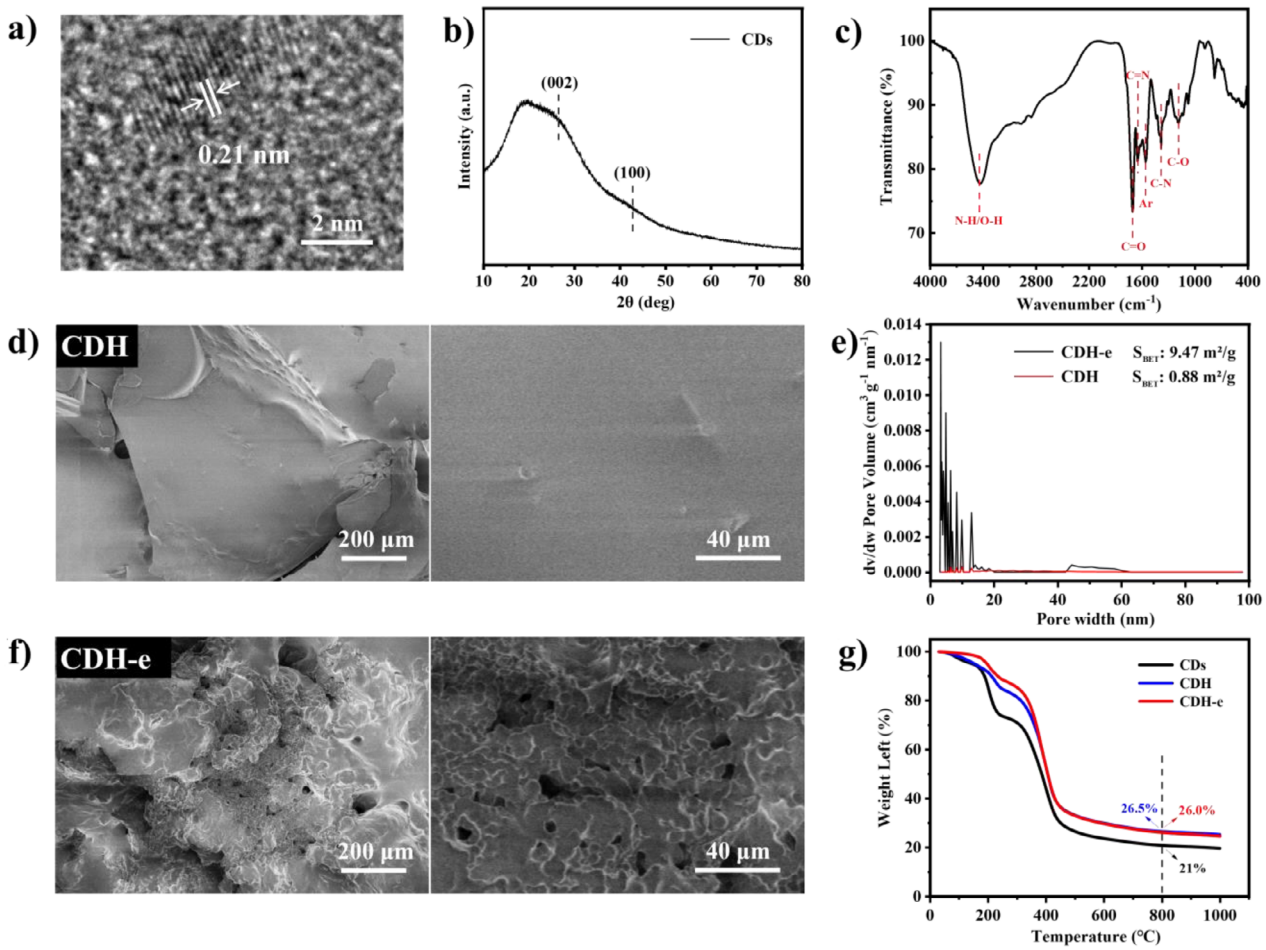

Figure 1. a) HRTEM images, b) XRD patterns, and c) FTIR spectra of CDs. d) SEM images of CDH. e) Pore size distributions calculated by the DFT method. f) SEM images of CDH-e. g) TG curves of CDs, CDH, and CDH-e.

© 2025 Wiley-VCH GmbH

15213773, 2025, 50, Downloaded from https://onlinelibrary.wiley.com/doi/10.1002/anie.202519704 by Huan-Ming Xiong - Fudan University , Wiley Online Library on [12/12/2025]. See the Terms and Conditions (https://onlinelibrary.wiley.com/terms-and-conditions) on Wiley Online Library for rules of use; OA articles are governed by the applicable Creative Commons License

of these samples primarily corresponds to the evaporation of the residual moisture in the system. The temperature range of 150° to 300 °C is associated with the thermal decomposition of those surface organic groups, and CDs exhibit the much higher weight loss because their surface groups are more apt to be lost than those crosslinked in hydrogels, which demonstrates that pre-polymerization is crucial to the yield enhancement. Since CDH was not subjected to etching and washing, more organic small molecules remain adsorbed in comparison with CDH-e. The decomposition of these molecules leads to a faster mass loss of CDH than that of CDH-e below 400 °C. The DTG curves (Figure S7) show that the interval with the highest mass loss rate occurs between 300° and 500 °C, corresponding to the formation of carbon materials (dehydrogenation, aromatization, and carbonization), similar to those biomass calcination processes.[49] Beyond 500 °C, the mass change begins to level off, indicating that the samples' structures become stable after calcination. Based on the above characterization and analyses, we believe CDs play the key role in the pre-etching process, in which KOH breaks the amide bonds in CDs to generate numerous small fragments. After washing away these fragments and K species with water, the defects and pores in the hydrogel will transform into the desired sub-nanometer pores during the subsequent calcination process.

The morphologies of the porous carbon were studied by SEM and TEM, respectively, in comparison with the control samples. The CDH-e hydrogels were calcined at 700°, 800°, and 900 °C to obtain CCDHs (CCDH-700, CCDH-800, and CCDH-900), respectively. Their production yields are 14%, 12%, and 10%, respectively, which are distinguished among those of porous carbon in the literature. SEM images (Figure 2a,c,e) reveal that CCDHs have three-dimensional network structures with interconnected pores, while TEM images (Figure 2b,d,f) confirm these samples have stacked carbon structures and abundant micropores. To highlight the necessity of the etching step, one CDH hydrogel was immersed in 2 M KOH solution for 30 min at room temperature (not 90 °C), rinsed with water thoroughly, and then calcined at 800 °C. The as-prepared sample was named as Control I, which has a smooth sheet structure without any three-dimensional pores (Figure 2g). And its TEM images (Figure 2h) do not reveal any discernible micropores. Furthermore, to compare our CDs' self-template etching method with the traditional KOH activation route, another CDH hydrogel was treated in almost the same manner, except for the lack of a washing step. The unwashed hydrogel was then calcined under the same conditions to obtain the porous carbon called Control II. Although the resulting morphology and micropore structure of Control II are similar to those of CCDHs (Figure 2i,j), the production yield of Control II was below 1%, which means the residual KOH in the samples had corroded most of the carbon materials. Hence, both etching and washing steps are crucial to our method.

N_2 adsorption/desorption experiments were conducted to analyze the SSA and pore structure of the samples. As shown in Figure 3a, the pore sizes of CCDH-700, CCDH-800, and CCDH-900 are primarily concentrated in the range of 0.35–2.8 nm, with a significant distribution of sub-nanometer (0.5–1.0 nm). In contrast, Control II only exhibits a poor pore distribution below 0.5 nm. These samples all exhibit type I isotherms at low relative pressures ($P/P_0 < 0.01$), indicating micropore-dominated porous structures. CCDH-700, CCDH-800, and CCDH-900 demonstrate higher adsorption capacities, with corresponding SSAs of 2159.2, 2733.6, and 1742.4 $m^2\ g^{-1}$, respectively, while the SSAs of Control I and II are only 0.7 and 701.1 $m^2\ g^{-1}$, respectively (Figures 3b and S8; Table S2). XRD patterns of all porous carbons show a broad and low-intensity diffraction peak at approximately 24°, indicating their amorphous porous nature (Figure S9).[50] Their Raman spectra display typical D (around 1345 cm^{-1}) and G (around 1591 cm^{-1}) bands (Figure 3c), representing the disordered and the graphitic vibrations in carbon materials. The high I_D/I_G values arise from the poorly ordered carbon structures, which are often observed in the highly porous, curved carbon frameworks with asymmetric heteroatom substitution, consistent with the XRD results.[51–54] The SSAs of porous carbon and the proportion of micropores can be tuned by varying the temperature. At 900 °C, although the SSA significantly decreases, the micropore area ratio reaches an impressive 98.3% (Figure 3d,e). CCDH-800 exhibits the largest SSA (2733.6 $m^2\ g^{-1}$), a considerable micropore area ratio (92.5%), the unusual packing density (0.82 g cm^{-3}), and a high yield (12%), which are remarkable in the literature (Figure 3f).[2,8–10,55–59] Based on all the above results, we propose a formation mechanism for the microporous carbon (Figure 3g). First, during the pre-polymerization process, CDs self-assemble under hydrothermal conditions to form hydrogels with robust mechanical strength, providing a substrate for pore making. Second, the pre-etching step utilizes alkali to break amide bonds, releasing small fragments and producing vacancies (Figure 1e). Based on Table S1, it is observed that after etching, CDH transforms into CDH-e, with an increase in N content and a decrease in O content. Therefore, it can be inferred that the fragments removed during etching contain more oxygen-containing segments. Finally, calcination at high temperatures transforms the organic frameworks into porous carbon, and in the meantime, the numerous vacancies turn into micropores. Such a pre-polymerization and pre-etching mechanism endows the as-prepared sub-nanometer microporous carbon with high packing density, large SSA, high yield, and high micropore area ratio.

In the FTIR spectra (Figure S10), all porous carbon samples show vibration bands at approximately 3433, 1637, 1386, and 1135 cm^{-1}, corresponding to O─H/N─H, C═C/C═O, C─N, and C─O functional groups, respectively, retaining the characteristics of the CDs precursor. XPS data demonstrate the surface elemental composition of CCDH-800, including C 1s (285 eV), N 1s (401 eV), and O 1s (533 eV), with atomic contents of 83.8%, 2.7%, and 13.5%, respectively (Figure S11a and Table S3). Figure S11b–d exhibits the deconvoluted spectra for C 1s, N 1s, and O 1s, respectively. It is well known that pyridine and pyrrole N species can improve the capacitive performance by introducing electron donors, thereby providing more active sites,[48] while graphitic N species can alter the charge density on the carbon surface, further enhancing the conductivity of the carbon material.[60]

© 2025 Wiley-VCH GmbH

15213773, 2025, 50, Downloaded from https://onlinelibrary.wiley.com/doi/10.1002/anie.202519704 by Huan-Ming Xiong - Fudan University , Wiley Online Library on [12/12/2025]. See the Terms and Conditions (https://onlinelibrary.wiley.com/terms-and-conditions) on Wiley Online Library for rules of use; OA articles are governed by the applicable Creative Commons License

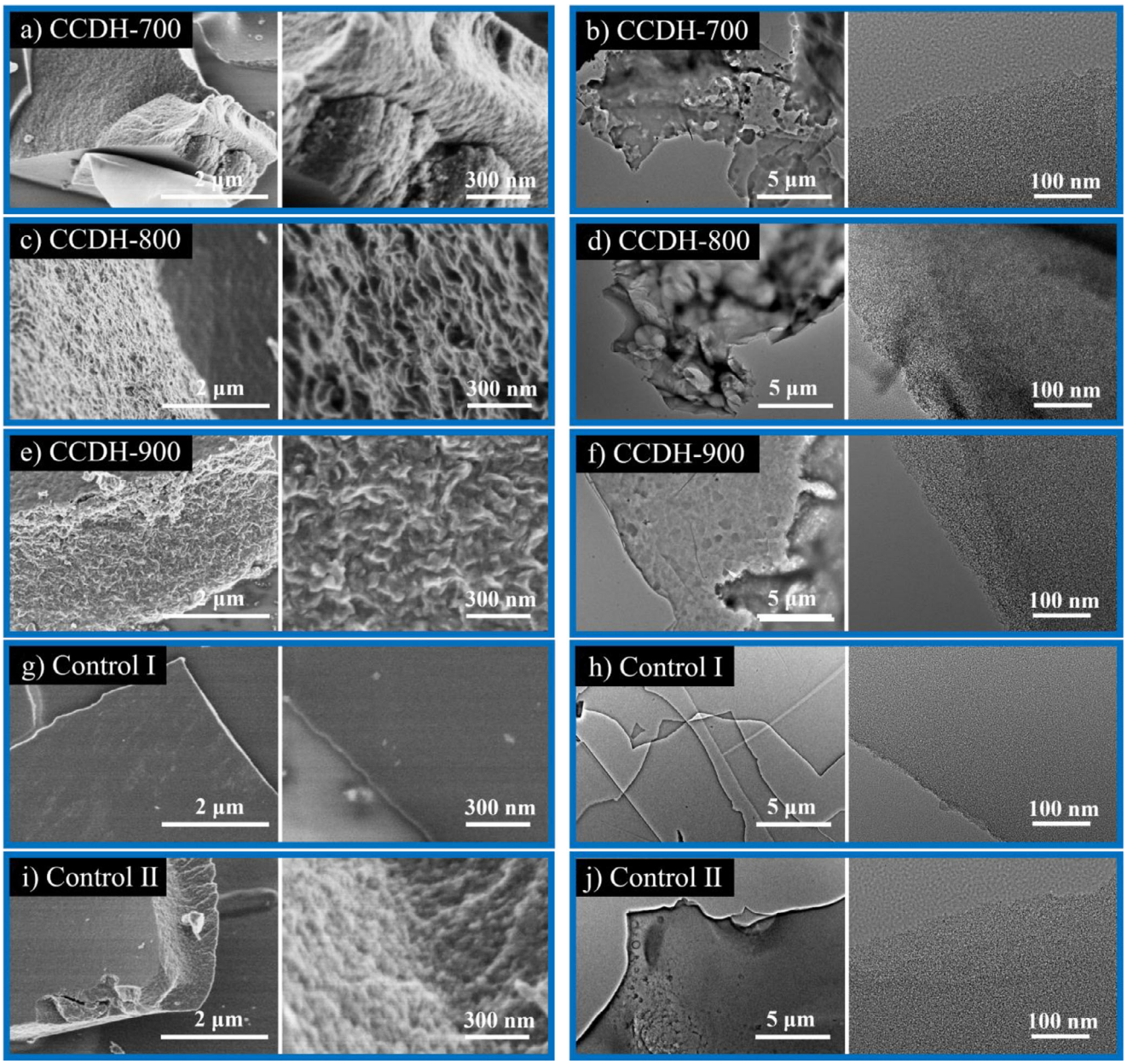

Figure 2. SEM (left) and TEM (right) images of a), b) CCDH-700, c), d) CCDH-800, e), f) CCDH-900, g), h) Control I, and i), j) Control II, respectively.

Additionally, oxygen-containing functional groups such as C─O─C and C─OH improve the wettability of the carbon, which increases the contact interface between the electrode and the electrolyte, thereby enhancing the capacitive performance of the porous carbon.[61] The XPS data of CCDH-700, CCDH-900, and Control I and II are also analyzed in the supporting information (Figures S12–S15 and Table S3). The N and O contents in CCDHs show a significant decrease compared to Control I, indicating a substantial loss of functional groups during the etching process, which supports the deamidation process mentioned in Figure 3g. In addition, the ratio of N to O gradually decreases with the increase in calcination temperature in CCDHs. However, even for CCDH-900, which has the lowest content of N and O, it is still higher than those of Control II. This result indicates that our self-template pre-etching process is milder than the conventional activation route, especially facilitating the in situ doping of N and O. It is well known that the heteroatoms in carbon electrodes are the main providers of the pseudocapacitance and are able to improve charge transport by enhancing the hydrophilicity of electrodes.[62,63]

We evaluated the capacitive performance of CCDH-800, which possesses the highest SSA, using 6 M KOH, 4 M H_2SO_4, and 1 M Na_2SO_4 aqueous solutions as electrolytes, respectively. Tests were first conducted under a low mass loading of 1 mg cm^{-2} in a three-electrode configuration, including galvanostatic charge–discharge (GCD), cyclic voltammetry (CV), and electrochemical impedance spectroscopy (EIS). As shown in Figure 4a–c, all GCD curves exhibit a typical triangular shape with no apparent IR drop. The optimal

© 2025 Wiley-VCH GmbH

15213773, 2025, 50, Downloaded from https://onlinelibrary.wiley.com/doi/10.1002/anie.202519704 by Huan-Ming Xiong - Fudan University , Wiley Online Library on [12/12/2025]. See the Terms and Conditions (https://onlinelibrary.wiley.com/terms-and-conditions) on Wiley Online Library for rules of use; OA articles are governed by the applicable Creative Commons License

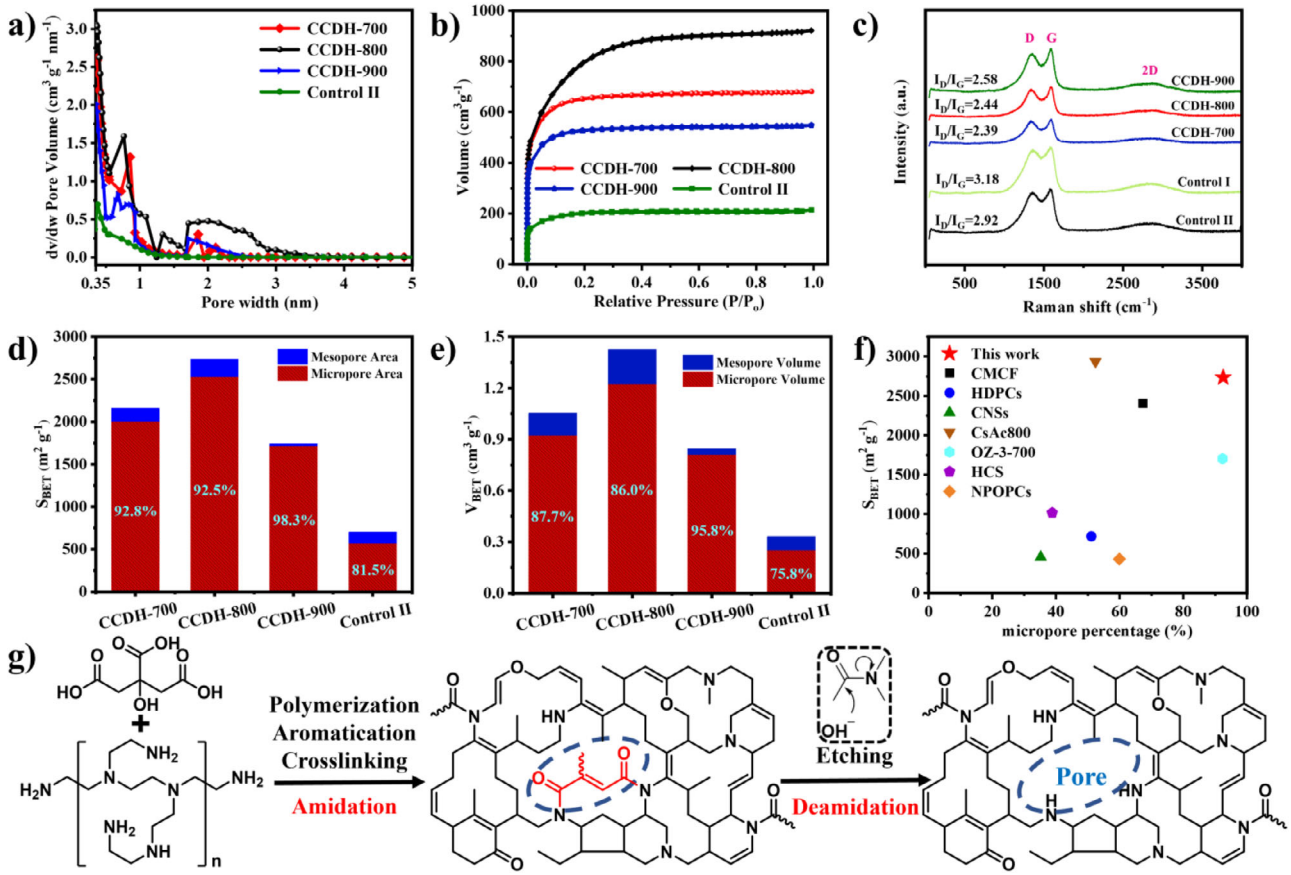

Figure 3. a) Pore size distributions, b) N_2 adsorption/desorption isotherms, c) Raman spectra, d) SSAs, and e) specific pore volumes of different samples, respectively. f) The comparison of CCDH-800 with other porous carbon materials in the literature. g) Proposed mechanism of the pore-forming process.

specific capacitance of CCDH-800 reached 639, 320, and 366 F g^{-1} in acidic, neutral, and alkaline electrolytes, respectively, outperforming many other carbon materials reported in the literature (Table S4). In Figures 4d–f, the steep slopes of the CV curves near the switching potentials indicate the low mass transfer resistance. With the scan rate increasing from 5 to 200 mV s^{-1}, the current density rises significantly, and all CV curves maintain quasi-rectangular shapes. Notably, the CV curves in acidic electrolytes remain relatively unchanged even at a high scan rate of 500 mV s^{-1}. In alkaline and neutral electrolytes, the absence of prominent peaks in CV curves suggests that the capacitance primarily arises from the electric double-layer capacitance (EDLC). But in the acidic electrolyte, CCDH-800 displays broad and symmetrical redox peaks, which are the characteristic of Faradaic capacitance (pseudocapacitance) derived from redox reactions involving pyrrolic N, pyridinic N, and oxygen-containing functional groups (Figure S11c,[64,65] The rate performance of CCDH-800 was calculated according to GCD curves, that retains over 70% of its capacity across all electrolytes at a current density of 20 A g^{-1} (Figure 4g). Figure 4h illustrates the cycling stability of CCDH-800 in acidic, neutral, and alkaline electrolytes after 10 000 cycles at 5 A g^{-1}, with the retention rates of 96.2%, 61%, and 87.9%, respectively. The different performances of capacitance and cycling stability in different electrolytes were further analyzed by EIS (Figures 4i, S16, and S17; Table S5). The fitted charge transfer resistance (R_{ct}) in H_2SO_4 is very low, while that in KOH is slightly larger, but the R_{ct} in Na_2SO_4 is several times larger than that in H_2SO_4. This discrepancy arises from the insufficient transport of hydrated K^+ or Na^+ ions through the meso-/macro-porous structures, while the smaller H_3O^+ ions can transport much more easily.

In the optimal H_2SO_4 electrolyte, the effect of mass loading was further investigated. As shown in Figure S18, when the mass loading of CCDH-800 increases tenfold, the specific capacitance retention remains above 84%, surpassing many comparable carbon materials (Table S6). Owing to the highly microporous structure (S_{micro}/S_{total} > 92.5%), CCDH-800 has a high packing density (0.82 g cm^{-3}), possessing the outstanding areal and volumetric specific capacitance of 5.4 F cm^{-2} and 443.9 F cm^{-3} at 1 A g^{-1}, respectively.[66] Although the specific capacitance gradually decreases with increasing current density, the reduction trend is moderate, and 81% of the initial capacity remains at 10 A g^{-1}. The CV curves still exhibit quasi-rectangular shapes similar to those at lower mass loading, while GCD curves maintain well-defined triangular shapes with an IR drop of only 0.06 V at 5 A g^{-1} (Figure S19). Similarly, after 10 000 cycles at 5 A g^{-1}, CCDH-800 shows a specific capacitance retention of 98.8% and a coulombic efficiency of 100% (Figure S20). Finally, EIS analysis was

© 2025 Wiley-VCH GmbH

15213773, 2025, 50, Downloaded from https://onlinelibrary.wiley.com/doi/10.1002/anie.202519704 by Huan-Ming Xiong - Fudan University , Wiley Online Library on [12/12/2025]. See the Terms and Conditions (https://onlinelibrary.wiley.com/terms-and-conditions) on Wiley Online Library for rules of use; OA articles are governed by the applicable Creative Commons License

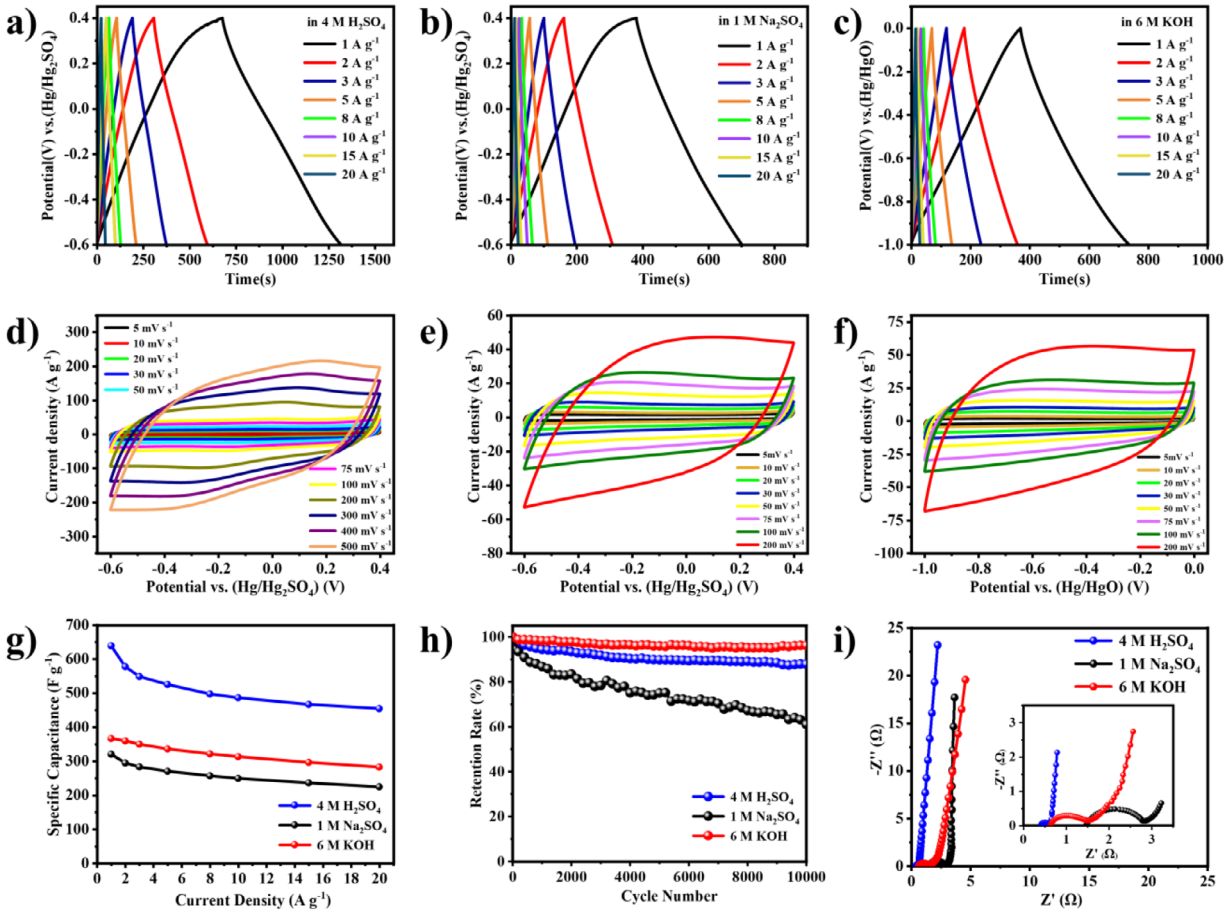

Figure 4. Electrochemical performances of CCDH-800 in a three-electrode system. GCD curves at different current densities in a) acidic, b) neutral, and c) alkaline aqueous solutions, respectively. d)–f) CV curves at various scan rates in the above three different aqueous solutions, respectively. g) The rate performance at various current densities, h) cycling stability for 10 000 cycles at 5 A g^{-1}, and i) Nyquist plots in different electrolytes, respectively.

conducted to explore the effect of high mass loading on charge transport (Figure S21), which reveals that, even with the heavily increased electrode thickness, neither the charge storage capacities nor the ion transport kinetics of the carbon electrodes are significantly impaired.

The optimal CCDH-800 was assembled into symmetric supercapacitors (SSCs), which exhibit a wide operating voltage range (1.3 V in the acidic and the alkaline electrolytes and 1.7 V in the neutral electrolyte) across a broad range of pH values. The CV curves measured at scan rates from 5 to 200 mV s^{-1} consistently show the ideal quasi-rectangular shape (Figure S22a–c), indicating an excellent charge–discharge reversibility and good electrochemical stability. At different current densities, all GCD curves of the SSCs display symmetric triangular shapes (Figure S23 a–c), confirming their ideal electrochemical reversibility and Coulombic efficiency. The specific capacitances calculated from the GCD curves are shown in Figure 5a. At 1 A g^{-1}, the results in acidic, neutral, and alkaline electrolytes are 138.5, 109.8, and 67.8 F g^{-1}, respectively. When the current density increases to 20 A g^{-1}, the retention rates of these samples are 65%, 64%, and 77%, respectively. Besides, such SSCs exhibit excellent cycling stability, maintaining 98.3%, 81.5%, and 96.0% capacitance retention after 10 000 cycles at a current density of 5 A g^{-1} in 4 M H_2SO_4, 1 M Na_2SO_4, and 6 M KOH solutions, respectively (Figure 5b). The Nyquist plots show only minor changes compared to the initial state (Figure S24), indicating a good electrochemical cycle stability. Moreover, in acidic, neutral, and alkaline conditions, the energy densities of the SSCs achieve 32.5, 44.1, and 15.9 Wh kg^{-1}, respectively, which are several times higher than those of many other aqueous SSCs in the literature (Figure 5c).[57,67–74] Therefore, our sub-nanometer microporous carbon material not only exhibits strong energy storage capability but also shows excellent compatibility with aqueous electrolytes over a wide pH range. When the mass loading of each single electrode is raised from 1 to 10 mg cm^{-2} the SSCs exhibit over 88% of the capacitance retention in acidic electrolytes (Figure 5d) and excellent rate performance (Figure S25). After 10 000 cycles, the capacitance retention is 99.8%, and the Nyquist plot shows little difference before and after cycling, implying an outstanding cycle stability (Figures 5e and S26).

Finally, the self-discharge behavior is an inherent shortcoming for supercapacitors. Our SSCs were charged to 1.3 or 1.7 V, and then their self-discharge behaviors were recorded

© 2025 Wiley-VCH GmbH

15213773, 2025, 50, Downloaded from https://onlinelibrary.wiley.com/doi/10.1002/anie.202519704 by Huan-Ming Xiong - Fudan University , Wiley Online Library on [12/12/2025]. See the Terms and Conditions (https://onlinelibrary.wiley.com/terms-and-conditions) on Wiley Online Library for rules of use; OA articles are governed by the applicable Creative Commons License

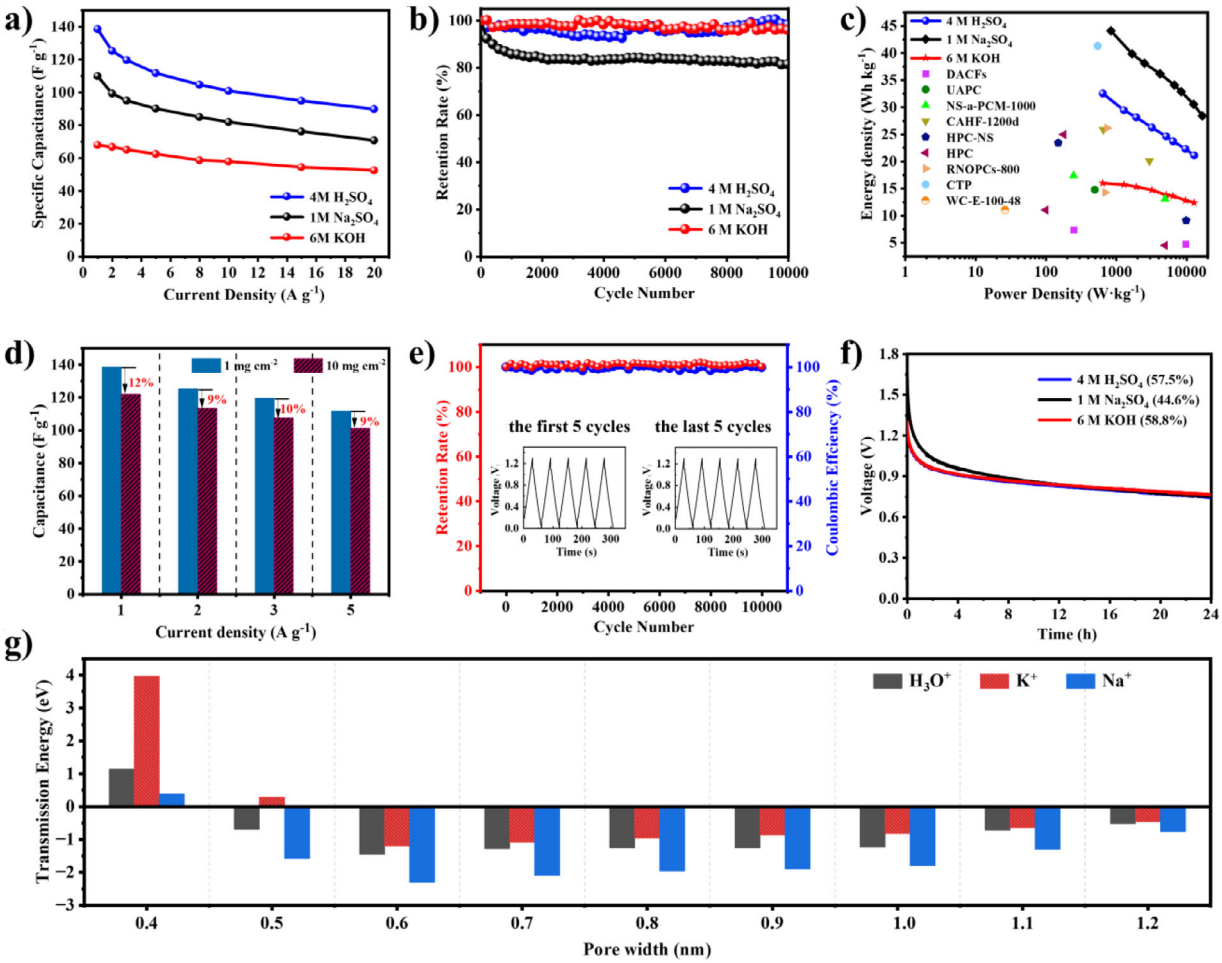

Figure 5. Electrochemical performances of CCDH-800//CCDH-800 SSCs in different electrolytes. a) specific capacitance at various current densities. b) Cycling stability at 5 A g^{-1} for 10 000 cycles. c) Ragone plot of power density versus energy density for CCDH-800//CCDH-800 SSCs and other carbon-based symmetric devices. d) Comparison of specific capacitance between single-electrode mass loading of 1 and 10 mg cm^{-2}. e) Cycling stability at 4 A g^{-1} for 10 000 cycles. (Insets are the GCD curves of the first and last five cycles.) f) Self-discharge curves of the SSCs. g) DFT simulations of different ions diffusing from infinity to the center of pores.

over 24 h in different electrolytes (Figure 5f). These devices exhibit initial voltage drops of 0.40, 0.34, and 0.39 V over the first 4 h, followed by slower voltage drops of 0.15, 0.20, and 0.15 V over the next 20 h, respectively. And thus, their retention rates after 24 h are 57.5%, 44.6%, and 58.8%, respectively, which can be ascribed to the inhibition of ion desorption by the dominant sub-nanometer pores. To elucidate the effect of pore size on the ion transport, the dynamic transmission energies of H^+, K^+, and Na^+ ions diffusing from infinity to the center of the pores were calculated using the DFT. The calculations were performed on the double-layer graphene structures that have varying interlayer distances to simulate pore channel structures with pore sizes from 0.4 to 1.0 nm (Figure 5g). The results show that when the pore width is below 0.5 nm, a high energy barrier emerges, indicating an unfavorable entry for the desolvated ions. As the pore size increases, the interaction energy reaches the minimum at 0.6 nm and increases gradually afterwards, indicating 0.5–1.0 nm is beneficial for the ion diffusion. Particularly, the change gradient of K^+ is the largest, corresponding to the strongest diffusion driving force; that is why SSCs have the best rate performance in the KOH electrolyte. The sub-nanometer (0.5–1.0 nm) pores in CCDH-800 are precisely within this energy trough region, leading to a synergistic enhancement in the specific capacitance and the charging dynamics.

Conclusion

We have invented a facile and reliable method for synthesizing porous carbon materials with ultra-large SSA, high micropore ratio, high packing density, rich heteroelements, functional surfaces, and decent production yield. This method is based on pre-polymerization of CDs, followed by pre-etching the obtained CD hydrogels. The pre-polymerization improves the carbon yield by crosslinking the surface groups of CDs, while the pre-etching process facilitates the formation of sub-nanometer pores with high SSA after the subsequent calcination. Such a sub-nanometer-pore-dominated structure satisfies the special requirements of ion desolvation/adsorption for high-performance supercapacitors. As

© 2025 Wiley-VCH GmbH

15213773, 2025, 50, Downloaded from https://onlinelibrary.wiley.com/doi/10.1002/anie.202519704 by Huan-Ming Xiong - Fudan University , Wiley Online Library on [12/12/2025]. See the Terms and Conditions (https://onlinelibrary.wiley.com/terms-and-conditions) on Wiley Online Library for rules of use; OA articles are governed by the applicable Creative Commons License

a result, the optimized material exhibits excellent specific capacitance in various acidic, neutral, and alkaline electrolytes. In neutral electrolytes, the assembled SSCs achieve the highest energy density of 30.5 Wh kg^{-1} at 12750 W kg^{-1}. In acidic electrolytes, 88% of the energy density is retained under a high mass loading of 10 mg cm^{-2}. In alkaline electrolytes, a superior rate performance is achieved with a capacitance retention of 77%. All of the above SSCs exhibit low self-discharge behaviors in aqueous solutions because of the confined ion diffusion by the special sub-nanometer pores, as predicted by DFT calculations. Overall, our present work provides new insights on the design, preparation, and optimization of sub-nanometer porous carbon materials, which exhibit excellent electrochemical properties in supercapacitors.

Acknowledgements

This work was financially supported by the National Natural Science Foundation of China (U24A20565, 22575057, 2225201), the Science and Technology Commission of Shanghai Municipality (25ZR1401024), and the Shanghai Pilot Program for Basic Research-Fudan University (21TQ1400100(21TQ009)).

Conflict of Interests

The authors declare no conflict of interest.

Data Availability Statement

The data that support the findings of this study are available in the supplementary material of this article.

Keywords: Carbon dots · Microporous carbon · Self-template · Sub-nanometer · Supercapacitors

[1] J. X. Li, Y. L. Xu, P. Z. Li, A. Voelkel, F. I. Saldaña, M. Antonietti, N. López-Salas, M. Odziomek, *Adv. Mater.* **2024**, *36*, 2311655, https://doi.org/10.1002/adma.202311655.
[2] J. L. Huang, Y. Q. Chen, Z. H. Cen, T. Yi, M. Liang, Y. L. Zhu, R. L. Liu, R. W. Fu, S. H. Liu, D. C. Wu, *Adv. Mater.* **2024**, *36*, 2403033, https://doi.org/10.1002/adma.202403033.
[3] J. H. Lee, N. D. Loh, Z. Y. Yeo, Y. K. Ong, D. Balakrishnan, C. M. A. Limpo, A. Datta, C. Cetin, S. C. Ning, C. Wong, J. Shi, F. C. Hou, J. H. Lin, T. Minamikawa, T. Ito, H. Kamisuki, S. Pennycook, P. Matsudaira, B. Özyilmaz, *Adv. Mater.* **2024**, *36*, 2402628, https://doi.org/10.1002/adma.202402628.
[4] P. Tang, W. Y. Tan, F. Z. Li, S. Xue, Y. H. Ma, P. W. Jing, Y. H. Liu, J. Zhu, X. B. Yan, *Adv. Mater.* **2023**, *35*, 2209186, https://doi.org/10.1002/adma.202209186.
[5] Q. Q. Yao, P. Tang, S. Y. Xie, Y. C. Chen, Q. Y. Dou, J. Zhu, X. B. Yan, *Adv. Funct. Mater.* **2024**, *34*, 2314962, https://doi.org/10.1002/adfm.202314962.
[6] B. L. Sun, N. Wang, X. C. Xie, L. Zhong, L. X. He, M. L. Xiang, K. Liang, W. C. Hu, *Angew. Chem. Int. Ed.* **2024**, *63*, e202408569, https://doi.org/10.1002/anie.202408569.
[7] A. M. M. Hasan, S. Bose, R. Roy, J. D. Marquez, C. Sharma, J. C. Nino, K. O. Kirlikovali, O. K. Farha, A. M. Evans, *Adv. Mater.* **2024**, *36*, 2405924, https://doi.org/10.1002/adma.202405924.
[8] J. Du, Q. Han, Y. Chen, M. Peng, L. Xie, A. Chen, *Angew. Chem. Int. Ed.* **2024**, *63*, 202411066, https://doi.org/10.1002/anie.202411066.
[9] J. X. Li, J. Kossmann, K. Zeng, K. Zhang, B. J. Wang, C. Weinberger, M. Antonietti, M. Odziomek, N. López-Salas, *Angew. Chem. Int. Ed.* **2023**, *135*, e202217808, https://doi.org/10.1002/ange.202217808.
[10] S. J. Guan, J. X. Li, Y. Y. Wang, Y. Yang, X. Zhu, D. D. Ye, R. Chen, Q. Liao, *Adv. Mater.* **2023**, *35*, 2304465, https://doi.org/10.1002/adma.202304465.
[11] N. Fechler, T.-P. Fellinger, M. Antonietti, *Adv. Mater.* **2013**, *25*, 75–79, https://doi.org/10.1002/adma.201203422.
[12] G. Singh, J. Lee, A. Karakoti, R. Bahadur, J. Yi, D. Zhao, K. Albahily, A. Vinu, *Chem. Soc. Rev.* **2020**, *49*, 4360–4404, https://doi.org/10.1039/D0CS00075B.
[13] J. Chmiola, G. Yushin, Y. Gogotsi, C. Portet, P. Simon, P. L. Taberna, *Science* **2006**, *313*, 1760–1763, https://doi.org/10.1126/science.1132195.
[14] H. R. Li, Z. T. Wu, X. C. Liu, H. T. Lu, W. C. Zhang, F. B. Li, H. Y. Yu, J. Y. Yu, B. Y. Zhang, Z. X. Xiong, Y. Tao, Q. H. Yang, *Nati. Sci. Rev.* **2024**, *11*, nwae207, https://doi.org/10.1093/nsr/nwae207.
[15] M. R. Zhang, T. Z. Xu, D. Wang, T. Y. Yao, Z. M. Xu, Q. S. Liu, L. F. Shen, Y. Yu, *Adv. Mater.* **2023**, *35*, 2209963, https://doi.org/10.1002/adma.202209963.
[16] W. Tian, H. Zhang, X. Duan, H. Sun, G. Shao, S. Wang, *Adv. Funct. Mater.* **2020**, *30*, 1909265, https://doi.org/10.1002/adfm.201909265.
[17] J. Wang, S. Kaskel, *J. Mater. Chem.* **2012**, *22*, 23710–23725, https://doi.org/10.1039/C2JM34066F.
[18] R. M. Navarro, M. A. Peña, J. L. G. Fierro, *Chem. Rev.* **2007**, *107*, 3952–3991, https://doi.org/10.1021/cr0501994.
[19] D. W. Kim, H. S. Kil, K. Nakabayashi, S. H. Yoon, J. Miyawaki, *Carbon* **2017**, *114*, 98–105, https://doi.org/10.1016/j.carbon.2016.11.082.
[20] K. Suresh Kumar Reddy, A. Al Shoaibi, C. Srinivasakannan, *New Carbon Mater.* **2012**, *27*, 344–351, https://doi.org/10.1016/S1872-5805(12)60020-1.
[21] G. Lin, R. Ma, Y. Zhou, Q. Liu, X. Dong, J. Wang, *Electrochim. Acta* **2018**, *261*, 49–57, https://doi.org/10.1016/j.electacta.2017.12.107.
[22] K. Zou, Y. Deng, J. Chen, Y. Qian, Y. Yang, Y. Li, G. Chen, *J. Power Sources* **2018**, *378*, 579–588, https://doi.org/10.1016/j.jpowsour.2017.12.081.
[23] M. A. Lillo Ródenas, D. Lozano-Castelló, D. Cazorla-Amorós, A. L. Solano, *Carbon* **2001**, *39*, 751–759, https://doi.org/10.1016/S0008-6223(00)00186-X.
[24] M. Sevilla, A. B. Fuertes, *J. Mater. Chem. A* **2013**, *1*, 13738, https://doi.org/10.1039/c3ta13149a.
[25] M. Sevilla, A. B. Fuertes, *ACS Nano* **2014**, *8*, 5069–5078, https://doi.org/10.1021/nn501124h.
[26] S. Yu, N. Sun, L. Hu, L. Wang, Q. Zhu, Y. Guan, B. Xu, *J. Power Sources* **2018**, *405*, 132–141, https://doi.org/10.1016/j.jpowsour.2018.10.033.
[27] Z. J. Fan, Y. Liu, J. Yan, G. Q. Ning, Q. Wang, T. Wei, L. J. Zhi, F. Wei, *Adv. Energy Mater.* **2012**, *2*, 419–424, https://doi.org/10.1002/aenm.201100654.
[28] H. W. Liang, W. Wei, Z. S. Wu, X. L. Feng, K. Müllen, *J. Am. Chem. Soc.* **2013**, *135*, 16002–16005, https://doi.org/10.1021/ja407552k.
[29] Y. Liu, Z. R. Wang, W. Teng, H. W. Zhu, J. X. Wang, A. A. Elzatahry, D. Al-Dahyan, W. Li, Y. H. Deng, D. Y. Zhao, *J. Mater. Chem. A* **2018**, *6*, 3162–3170, https://doi.org/10.1039/C7TA10106F.

© 2025 Wiley-VCH GmbH

15213773, 2025, 50, Downloaded from https://onlinelibrary.wiley.com/doi/10.1002/anie.202519704 by Huan-Ming Xiong - Fudan University , Wiley Online Library on [12/12/2025]. See the Terms and Conditions (https://onlinelibrary.wiley.com/terms-and-conditions) on Wiley Online Library for rules of use; OA articles are governed by the applicable Creative Commons License

[30] J. Wei, D. D. Zhou, Z. K. Sun, Y. H. Deng, Y. Y. Xia, D. Y. Zhao, *Adv. Funct. Mater.* **2013**, *23*, 2322–2328, https://doi.org/10.1002/adfm.201202764.
[31] M. Sevilla, N. Díez, A. B. Fuertes, *ChemSusChem* **2021**, *14*, 94–117, https://doi.org/10.1002/cssc.202001838.
[32] B. Yan, H. Huang, X. Qin, S. Xiu, J. Choi, D. Ko, T. Chen, W. Zhang, B. Quan, G. Diao, X. Jin, Y. Piao, *ACS Appl. Energy Mater.* **2021**, *4*, 13735, https://doi.org/10.1021/acsaem.1c02463.
[33] H. Peng, S. Qi, Q. Miao, R. Zhao, Y. Xu, G. Ma, Z. Lei, *J. Power Sources* **2021**, *482*, 228993, https://doi.org/10.1016/j.jpowsour.2020.228993.
[34] S. Wang, J. Miao, B. Ren, Y. Xu, Z. Tian, L. Zhang, Z. Liu, *J. Alloys Compd.* **2022**, *920*, 165946, https://doi.org/10.1016/j.jallcom.2022.165946.
[35] H. Ouyang, C. Fang, Z. Xu, L. Li, G. Xiao, *Nanoscale* **2022**, *14*, 11298–11304, https://doi.org/10.1039/D2NR01655A.
[36] Y. J. Li, G. L. Wang, T. Wei, Z. J. Fan, P. Yan, *Nano Energy* **2016**, *19*, 165–175, https://doi.org/10.1016/j.nanoen.2015.10.038.
[37] Z. Ling, Z. Y. Wang, M. D. Zhang, C. Yu, G. Wang, Y. F. Dong, S. H. Liu, Y. W. Wang, J. S. Qiu, *Adv. Funct. Mater.* **2016**, *26*, 111–119, https://doi.org/10.1002/adfm.201504004.
[38] Y. Zhang, Q. Ma, H. Li, Y. W. Yang, J. Luo, *Small* **2018**, *14*, 1800133, https://doi.org/10.1002/smll.201800133.
[39] M. Sevilla, G. A. Ferrero, N. Diez, A. B. Fuertes, *Carbon* **2018**, *131*, 193–200, https://doi.org/10.1016/j.carbon.2018.02.021.
[40] L. Ai, W. J. Xiang, J. P. Xiao, H. M. Liu, J. K. Yu, L. L. Zhang, X. T. Wu, X. L. Qu, S. Y. Lu, *Adv. Mater.* **2024**, *36*, 2401220, https://doi.org/10.1002/adma.202401220.
[41] J. Li, H. Zhou, S. Jin, B. Xu, Q. Teng, C. H. Li, J. S. Li, Q. J. Li, Z. H. Gao, C. F. Zhu, Z. F. Wang, W. Su, F. L. Yuan, *Adv. Mater.* **2024**, *36*, 2401493, https://doi.org/10.1002/adma.202401493.
[42] Q. Cheng, T. Zhang, Q. Wang, X. Wu, L. Li, R. Lin, Y. Zhou, S. Qu, *Adv. Mater.* **2024**, *36*, 2408685, https://doi.org/10.1002/adma.202408685.
[43] X. R. Zhang, T. B. Song, T. L. He, Q. L. Ma, Z. F. Wu, Y. G. Wang, H. M. Xiong, *Adv. Funct. Mater.* **2025**, *35*, 2419219, https://doi.org/10.1002/adfm.202419219.
[44] J. S. Wei, C. Ding, P. Zhang, H. Ding, X. Q. Niu, Y. Y. Ma, C. Li, Y. G. Wang, H. M. Xiong, *Adv. Mater.* **2019**, *31*, 1806197, https://doi.org/10.1002/adma.201806197.
[45] H. S. Hou, C. E. Banks, M. J. Jing, Y. Zhang, X. B. Ji, *Adv. Mater.* **2015**, *27*, 7861–7866, https://doi.org/10.1002/adma.201503816.
[46] L. B. Tang, R. B. Ji, X. M. Li, G. X. Bai, C. P. Liu, J. H. Hao, J. Y. Lin, H. X. Jiang, K. S. Teng, Z. B. Yang, S. P. Lau, *ACS Nano* **2014**, *8*, 6312–6320, https://doi.org/10.1021/nn501796r.
[47] L. Li, Y. T. Li, Y. Ye, R. T. Guo, A. N. Wang, G. Q. Zou, H. S. Hou, X. B. Ji, *ACS Nano* **2021**, *15*, 6872–6885, https://doi.org/10.1021/acsnano.0c10624.
[48] D. Hulicova-Jurcakova, M. Seredych, G. Q. Lu, T. J. Bandosz, *Adv. Funct. Mater.* **2009**, *19*, 438–447, https://doi.org/10.1002/adfm.200801236.
[49] B. Babinszki, E. Jakab, V. Terjek, Z. Sebestyen, G. Varhegyi, Z. May, A. Mahakhant, L. Attanatho, A. Suemanotham, Y. Thanmongkhon, Z. Czegeny, *J. Anal. Appl. Pyrolysis* **2021**, *155*, 105069, https://doi.org/10.1016/j.jaap.2021.105069.
[50] L. N. Han, X. Wei, Q. C. Zhu, S. M. Xu, K. X. Wang, J. S. Chen, *J. Mater. Chem. A* **2016**, *4*, 16698–16705, https://doi.org/10.1039/C6TA05607E.
[51] D. H. Tang, T. Wang, W. T. Zhang, Z. Zhao, L. Zhang, Z. A. Qiao, *Angew. Chem. Int. Ed.* **2022**, *61*, e202203967, https://doi.org/10.1002/anie.202203967.
[52] P. Han, M. S. Cheng, D. H. Luo, W. Cui, H. C. Liu, J. G. Du, M. L. Wang, Y. P. Zhao, L. Chen, C. Z. Zhu, J. Xu, *Energy Storage Mater.* **2020**, *24*, 486–494, https://doi.org/10.1016/j.ensm.2019.07.009.
[53] J. Huang, C. Liu, Y. Z. Jin, J. C. Chen, *Chem. Eng. J.* **2023**, *461*, 141930, https://doi.org/10.1016/j.cej.2023.141930.
[54] N. F. Yu, H. Chen, J. B. Kuang, K. L. Bao, W. Yan, J. L. Ye, Z. T. Yang, Q. H. Huang, Y. P. Wu, S. G. Sun, *Nano Res.* **2022**, *15*, 7209–7219, https://doi.org/10.1007/s12274-022-4382-7.
[55] X. Y. Li, C. C. Cai, L. Zhou, L. Q. Mai, H. J. Fan, *Ad. Mater.* **2024**, *36*, 2404393, https://doi.org/10.1002/adma.202404393.
[56] J. Lu, X. Zhong, X. Lin, J. Gui, M. Zheng, Y. Liu, Y. Liang, *Energy Environ. Sci.* **2024**, *17*, 6833–6843, https://doi.org/10.1039/D4EE02163K.
[57] Q. Liu, D. L. Wu, T. Wang, C. G. Wang, D. Z. Jia, *Adv. Funct. Mater.* **2024**, *34*, 2400556, https://doi.org/10.1002/adfm.202400556.
[58] H. Jin, X. Feng, J. Li, M. Li, Y. Xia, Y. Yuan, C. Yang, B. Dai, Z. Lin, J. Wang, J. Lu, S. Wang, *Angew. Chem. Int. Ed.* **2019**, *58*, 2397–2401, https://doi.org/10.1002/anie.201813686.
[59] J. Du, Q. Han, Y. Chen, M. Peng, L. Xie, A. Chen, *Angew. Chem. Int. Ed.* **2024**, *63*, e202411066, https://doi.org/10.1002/anie.202411066.
[60] J. Du, Y. Zhang, H. Lv, A. Chen, *J. Alloys Compd.* **2021**, *853*, 157091, https://doi.org/10.1016/j.jallcom.2020.157091.
[61] L. Yang, T. Wang, D. Wu, *Chin. J. Chem.* **2020**, *38*, 1123–1131, https://doi.org/10.1002/cjoc.201900482.
[62] R. Zhang, X. X. Jing, Y. T. Chu, L. Wang, W. J. Kang, D. H. Wei, H. B. Li, S. L. Xiong, *J. Mater. Chem. A* **2018**, *6*, 17730–17739, https://doi.org/10.1039/C8TA06471G.
[63] Y. C. Liu, M. J. Shi, M. N. Han, J. Yang, J. H. Yu, M. Narayanasamy, K. Dai, S. Angaiah, C. Yan, *Chem. Eng. J.* **2020**, *387*, 124104, https://doi.org/10.1016/j.cej.2020.124104.
[64] Y. Li, L. Liu, Y. Wu, T. Wu, H. Wu, Q. Cai, Y. Xu, B. Zeng, C. Yuan, L. Dai, *J. Mater. Chem. A* **2019**, *7*, 13154–13163, https://doi.org/10.1039/C9TA00890J.
[65] B. Ding, D. Guo, Y. H. Wang, X. L. Wu, Z. J. Fan, *J. Power Sources* **2018**, *398*, 113–119, https://doi.org/10.1016/j.jpowsour.2018.07.063.
[66] L. Suarez, V. Barranco, T. A. Centeno, *J. Colloid Interface Sci.* **2021**, *588*, 705–712, https://doi.org/10.1016/j.jcis.2020.11.093.
[67] Q. Wang, F. Y. Liu, Z. Y. Jin, X. R. Qiao, H. C. Huang, X. Chu, D. Xiong, H. T. Zhang, Y. Liu, W. Q. Yang, *Adv. Funct. Mater.* **2020**, *30*, 2002580, https://doi.org/10.1002/adfm.202002580.
[68] J. C. Zhang, J. W. Luo, Z. X. Guo, Z. D. Liu, C. P. Duan, S. M. Dou, Q. Y. Yuan, P. Liu, K. M. Ji, C. H. Zeng, J. Xu, W. D. Liu, Y. A. Chen, W. B. Hu, *Adv. Energy Mater.* **2023**, *13*, 2203061, https://doi.org/10.1002/aenm.202203061.
[69] H. H. Lu, C. Yang, J. Chen, J. Li, H. L. Jin, J. C. Wang, S. Wang, *Small* **2020**, *16*, 1906584, https://doi.org/10.1002/smll.201906584.
[70] H. Wu, W. Y. Yuan, X. W. Yuan, L. F. Cheng, *Energy Storage Mater.* **2022**, *50*, 514–524, https://doi.org/10.1016/j.ensm.2022.05.046.
[71] L. Yao, J. S. Lin, Y. Y. Chen, X. J. Li, D. R. Wang, H. T. Yang, L. B. Deng, Z. J. Zheng, *InfoMat.* **2022**, *4*, e12278, https://doi.org/10.1002/inf2.12278.
[72] X. Y. Qian, L. Miao, J. X. Jiang, G. C. Ping, W. Xiong, Y. K. Lv, Y. F. Liu, L. H. Gan, D. Z. Zhua, M. X. Liu, *Chem. Eng. J.* **2020**, *388*, 124208, https://doi.org/10.1016/j.cej.2020.124208.
[73] J. Li, Z. H. Xia, X. W. Wang, C. Feng, Q. C. Zhang, X. A. Chen, Y. Yang, S. Wang, H. L. Jin, *Adv. Mater.* **2024**, *36*, 2310422, https://doi.org/10.1002/adma.202310422.
[74] F. Wang, J. Y. Cheong, J. Lee, J. Ahn, G. G. Duan, H. L. Chen, Q. Zhang, I. D. Kim, S. H. Jiang, *Adv. Funct. Mater.* **2021**, *31*, 2101077, https://doi.org/10.1002/adfm.202101077.

Manuscript received: September 08, 2025
Revised manuscript received: September 28, 2025
Manuscript accepted: September 29, 2025
Version of record online: October 07, 2025

© 2025 Wiley-VCH GmbH

15213773, 2025, 50, Downloaded from https://onlinelibrary.wiley.com/doi/10.1002/anie.202519704 by Huan-Ming Xiong - Fudan University , Wiley Online Library on [12/12/2025]. See the Terms and Conditions (https://onlinelibrary.wiley.com/terms-and-conditions) on Wiley Online Library for rules of use; OA articles are governed by the applicable Creative Commons License